RESEARCH PAPER

Unsaturated slopes behavior under antecedent intermittent rainfall patterns: centrifuge and numerical study

Sanchitha Hema Sharendra Jayakody[1] · Ryosuke Uzuoka[2] · Kyohei Ueda[2] · Jiawei Xu[3]

Abstract

Antecedent rainfall is a prime factor for rainfall-induced landslides on unsaturated slopes. The effects of the intermittent behavior of antecedent rainfall on landslide initiation are uncertain. The work described here had the objective of showing the influence of antecedent intermittent rainfall patterns to predict landslide initiation. Soil slope models prepared from silty sand were tested in centrifuge model testing. At first, soil slopes experienced different antecedent rainfall patterns, namely, uniform gap, decreasing gap, and increasing gap, before they were exposed to continuous rainfall until the failure was initiated. The seepage and deformation behaviors of instrumented slopes were evaluated and back-analyzed with soil–water–air coupled hydromechanical finite element analysis using calibrated material parameters and suitable boundary conditions. The evolution of porewater pressure, displacements, and deviatoric strains was found to provide comparable responses. The analysis of incremental velocity clearly showed that times for landslide initiation follow the order of decreasing gap, uniform gap, and increasing gap antecedent rainfall patterns. The study identified that not only cumulative rainfall, but also antecedent intermittent rainfall patterns have a significant effect as a triggering agent and suggested incorporating it as a parameter for landslide early warning mechanisms.

Keywords Antecedent intermittent rainfall patterns · Centrifuge modeling · Landslides · Numerical modeling · Unsaturated slope

1 Introduction

Changes in global climatic conditions and man-made actions have steered the occurrence of natural hazards and disasters so common all around the world. Among many, rainfall-induced landslides are one of the main geo-

✉ Sanchitha Hema Sharendra Jayakody
    jayakody.sharendra.51a@st.kyoto-u.ac.jp

    Ryosuke Uzuoka
    uzuoka.ryosuke.6z@kyoto-u.ac.jp

    Kyohei Ueda
    ueda.kyohei.2v@kyoto-u.ac.jp

    Jiawei Xu
    xjw023@chd.edu.cn

[1] Department of Civil and Earth Resources Engineering, Kyoto University, Kyoto, Japan

[2] Disaster Prevention Research Institute, Kyoto University, Kyoto, Japan

[3] School of Highway, Chang'an University, Xi'an, Shaanxi Province, China

disasters that happen endlessly and cause much damage to society in terms of socio-economic and environmental. A few recent catastrophic events were in 2016, followed by the Roanu cyclone, and a rapid and long traveling landslide was triggered at Aranayaka, Sri Lanka, resulting in 127 deaths and massive destruction to the surrounding establishments [12] and with 42 fatalities; another landslide happened in Shuicheng, China, in 2019 attributed to a continuous heavy rainfall [15]. In addition to the contribution of adverse geological and topography features to landslide initiation, owing to greater research over the last decades, it is widely proven that the loss of matric suction in unsaturated soil, development of porewater pressure, and saturation-dependent shear strength reduction are the primary failure mechanisms of rainfall triggered landslides. Considerable progress has been made to study the rainfall-induced landslides or slope failures by virtue of different methods such as large/small scale tests [35, 45]; instrumented field tests [1, 29, 32]; centrifuge model tests [3, 38, 39] and numerical simulations [8, 10, 28]. The

insight provided by the above is extremely helpful for the understanding of slopes' response to rainfall infiltration.

Spatial susceptibility and temporal predictability widely depend on the boundary conditions such as topography, soil layering, and slopes' initial condition in addition to the rainfall infiltration. Recent improvements in Geographic Information Systems (GIS) enable the combination of topography for predicting landslides using a hydrological-geotechnical framework [20, 22] and statistical methods [46]. The effect of layered soil on slope stability was examined using field instrumentation and numerical modeling to highlight the presence of heterogeneous soil profiles in field conditions [11]. The importance of slopes' initial conditions such as degree of saturation, slope angle, and porosity was underlined by employing centrifuge modeling [48]. Even though the above parameters are of utmost importance in slope stability, landslide early warning systems are usually implemented based on the actual rain gauge readings or forecasted rainfall and the correlations generated from past events. Researchers primarily select either rainfall intensity [18, 19, 21] or antecedent effective rainfall [54, 58] as the appropriate precipitation parameter. Referring to the rainfall data of many reported cases shows that there are significant fluctuations in rainfall intensity as well as the rainfall duration [15]. Landslides have occurred not only at the time of highest rainfall [49] but also a few hours later the maximum rainfall reported [12]. These observations elucidate that there is a rather significance on the antecedent rainfall than the intraday rainfall for a landslide to be triggered.

The importance of the antecedent rainfall conditions to the initiation of landslides has been emphasized by the studies [33, 34]. Primarily, numerical studies conducted by researchers illustrated how soil permeability could affect the significance of antecedent rainfall [33] and discussed how antecedent rainfall intensity patterns may result in a different factor of safety values [34]. Furthermore, the performance of the slopes under the different rainfall intensities and constant durations between rainfall events was examined [56]. However, an often overlooked and crucial factor is the intermittency of antecedent rainfall for landslide initiation which is rarely studied. Slopes' condition prior to a major rainfall could not be the same if the frequency of antecedent rainfall events is different while the slopes' experienced the same cumulative rainfall. This suggests that further studies are required depending on the intermittent behavior of antecedent rainfall to provide more understanding of landslide initiation. Therefore, in this study, it is hypothesized that not only cumulative rainfall, but also antecedent intermittent rainfall patterns have an impact on initiation in shallow slope failures. The objectives of this paper are (i) to experimentally test the above hypothesis using centrifuge model testing in which a total of four identical soil slopes are subjected to different rainfall conditions and (ii) to validate the observations and behavior of physical model results using finite element modeling and conduct an extended study to provide the relative importance of antecedent rainfall events.

2 Experimental method and materials

2.1 Centrifuge modeling

Physical modeling can be identified as the bridge between real scenarios and numerical modeling. In this paper, centrifuge modeling will be used as the physical modeling technique to discuss the effect of antecedent rainfall and its patterns on landslide initiation. To reproduce the soil behavior in terms of strength and stiffness, centrifuge modeling uses the concept of application of in situ stresses to the soil model by an enhanced gravitational acceleration field (N) [40] and thereby equalizes the stress so that the scale factor of linear dimensions (model: prototype) is 1: N. According to the scaling laws presented [17], the velocity of inertial actions is the same in both the model and prototype; thus, the time for the inertial events has a scale factor of 1: N. The centrifuge facility at Disaster Prevention Research Institute, Kyoto University, was used to model the slopes, and it has an effective radius of 2.5 ± 0.05 m. Therefore, the scale factor for suction could be taken as 01, since the ratio between the centrifuge arm length and the model height is comparatively large [13].

The objective of this paper is to discuss the effect of antecedent rainfall patterns on landslide initiation rather than reproducing a case history to quantify mobility or runout [36, 38]. Therefore, water was used as the pore fluid instead of a higher-viscosity fluid. The effect of the particle size scale factor is not taken into consideration [2, 37, 38] and the seepage flow experiences by the model during rainfall events has a time scale factor of 1: N^2 [13, 40]. The rainfall duration and the total rain in the model are scaled down by N^2 times and N times compared to the prototype. Accordingly, rainfall intensity is N times higher in the model scale [17, 39]. However, using water could result in the dissipation of excess porewater pressure $\sqrt{N}$ faster than in the prototype scale [2, 38]. This can provide the slopes to reinstate their stability much quicker [36]. The scaling laws used in these experiments are listed in Table 1. All the experimental results reported in this study are model scale unless otherwise stated.

Table 1 Centrifuge scaling laws used in the experiments

Parameter and dimension	Model/prototype
Stress $[ML^{-1}T^{-2}]$	1
Length [L]	$1/N$
Time (diffusion) [T]	$1/N^2$
Rainfall intensity $[LT^{-1}]$	N
Rainfall length [L]	$1/N$
Rainfall duration [T]	$1/N^2$
Rainfall frequency [1/T]	N^2
Hydraulic conductivity $[LT^{-1}]$	N

2.2 Test program

A total of four tests were carried out to discuss the impact of the gap between antecedent rainfall events on landslide triggering. As illustrated in Fig. 1, Test-01 was conducted
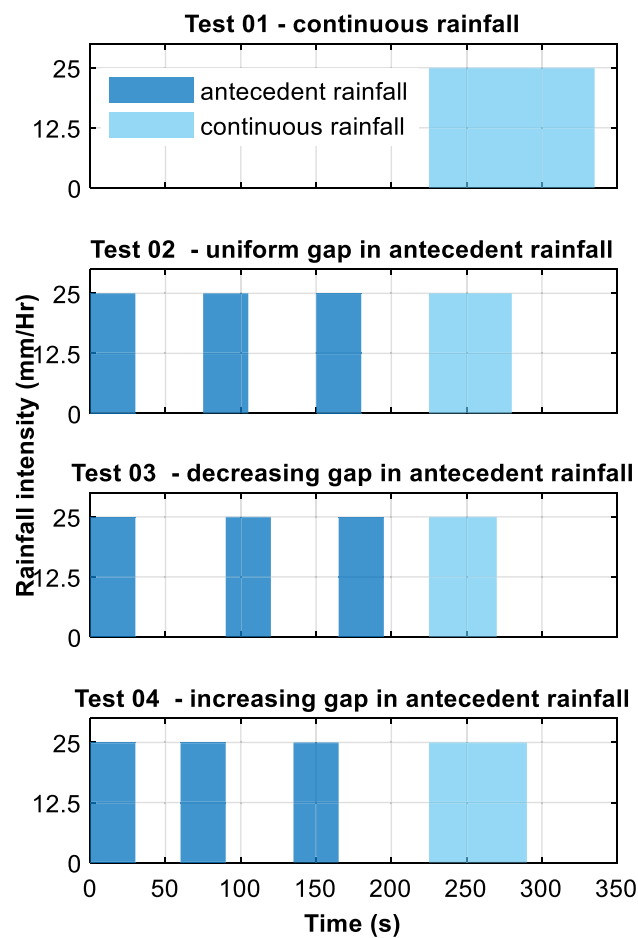
Fig. 1 Rainfall patterns used in the test program: Tests 02, 03, and 04 show the uniform, decreasing, and increasing time gaps between rainfall events; dark blue shows the antecedent rainfall, and light blue shows continuous rainfall (color figure online)

as the reference test for the test series in which the slope experienced only continuous rainfall until the failure. The antecedent rainfall patterns were conditioned as the events of rainfall and no rainfall. To achieve the same antecedent cumulative precipitation, rainfall intensity, and duration were kept constant while changing the gap between rainfall events in this test program. The scattered behavior of rainfall gaps was idealized as a uniform gap in Test-02 (45 s time interval between rainfall events), a decreasing gap in Test-03 (60 s → 45 s → 30 s time interval between rainfall events), and an increasing gap in Test-04 (30 s → 45 s → 60 s time interval between rainfall events). Rainfall was applied for 30 s in each antecedent rainfall event. The total antecedent time considered in these cases was 225 s, and all slopes were exposed to 90 s of accumulated rainfall. At 225 s, continuous rainfall was applied on the slopes until the failure occurred.

2.3 Slope material

Masado soil, which is commercially available in western Japan, was used as the slope material in this test program. The particle size distribution in Fig. 2 shows that the silt percentage of Masado soil is around 10%, and according to the American Society for Testing and Material classification system, soil can be categorized as well-graded sand with silt. The samples were used in this test series of dry density (γ_d) of 1.5 g/cm^3. The void ratio was maintained at 0.76 which is in the medium-dense state. The index properties of Masado soil are provided in Table 2.

2.4 Experimental setup

2.4.1 Boundary conditions

A rigid box, which has internal dimensions of $600 \times 300 \times 140$ mm, was employed as the model
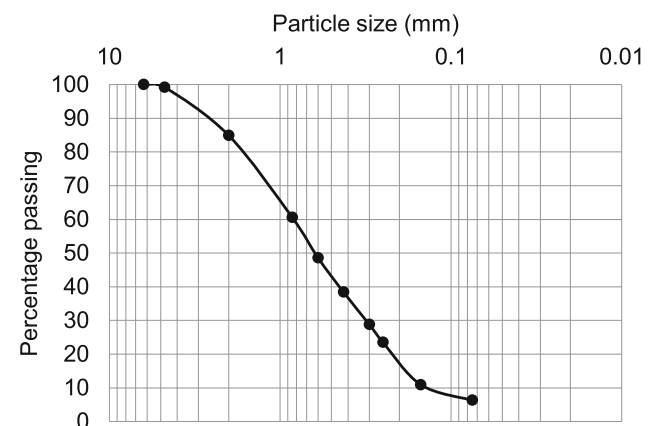
Fig. 2 Particle size distribution graph of Masado soil

Table 2 Index properties of Masado soil

Parameter	Value
D_{60}, D_{30}, D_{10} (mm)	0.83, 0.32, 0.15
Particle density (G_s) (g/cm^3)	2.65
Max dry density (g/cm^3) (γ_{dmax})	1.76
Optimum moisture content (%)	15.5

container. A schematic diagram of the rigid box is demonstrated in Fig. 3. In the model, the slope geometry and boundary conditions were designed to discuss the shallow slope failures and to avoid water storage at the toe of the slope. There were drainage holes to divert the water that seeped out from the slope to the drainage tank. The slope was constructed on an aluminum base, which acted as an impermeable boundary condition, and the sides of the aluminum base were properly sealed to avoid any seepage via the side boundaries. The slope was housed using the aluminum frame with nozzles attached to it.
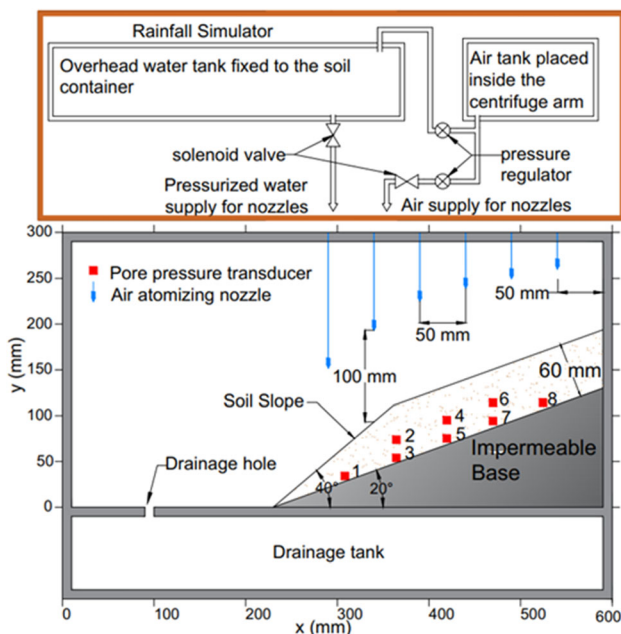
2.4.2 Rainfall simulation

Different methods were used to simulate rainfall boundary conditions in the centrifuge experiments such as nozzles arrangements [3, 27, 39], drip-type arrangements [47, 48] and spraying water onto the slope [25]. To reproduce the rainfall in the model, air pneumatic nozzles were used

Fig. 3 Schematic diagram of the centrifuge model with rainfall simulator: locations of the pore pressure transducers and air atomizing nozzles are shown

considering their potential to deliver rain droplets in an average size of 20 to 100 μm, which minimizes the impact pressure exerted on the slope surface. A total of 18 nozzles (03 rows × 06 columns) were utilized, and these were fixed on the top lid of the model container. The centrifuge apparatus rotates clockwise, and due to the Coriolis effect, there is a tendency that the spray mist to move opposite to the rotation and not reach the slope surface at higher gravity levels [41]. The nozzles were configured by changing the spacing among nozzles and the height between the nozzles and the slope to minimize the Coriolis effect. During these trial tests a bottom-sealed seeding tray was employed to collect and measure the rainfall distribution. The trial tests were conducted until rainfall covered the entire slope with an acceptable level of uniform spray distribution. Further, it was ensured that the rightmost nozzle would not create a seepage flow along the right-side boundary wall of the container. As illustrated in Fig. 3, pressurized air was supplied by an air tank placed in the centrifuge arm, and pressurized water was supplied by the water tank fixed to the model container. The applicability of this integrated system was discussed during previous studies [51]. Furthermore, several calibration tests were conducted to determine suitable air pressure and water pressure values to generate the desired rainfall intensity. In this test series, only 25 mm/Hr in the prototype scale, which is 1250 mm/Hr in the model scale, was applied on the slopes. An antecedent rainfall event lasted for 30 s in the model scale corresponding to a rainfall of 20 h in the prototype scale which accounts for a heavy rainfall condition. The antecedent rainfall patterns were achieved by a remote controller, which switches on/off the rainfall in the desired time intervals.

2.4.3 Slope construction

Before constructing the slope by the wet tamping method, a homogenized soil mixture was prepared by thoroughly mixing the calculated soil amount to a gravimetric water content of 10% and kept for about 24 h. The aluminum base was covered by sandpaper to provide enough friction between the soil and the base. The soil layers were built in 20 mm lifts and compacted uniformly to achieve the target bulk density of 1.65 g/cm^3. This is equivalent to a relative compaction of 85% (γ_d/γ_{dmax}). Each layer was scratched before placing the next layer to form uniform layers and proper shear connections among the layers. Before excess soil was scraped to form the required slope geometry, the compacted layers were covered using a polythene sheet and kept overnight to equalize. The schematic view of the slope geometry is shown in Fig. 3. All the tests were conducted under a centrifugal acceleration of 50 g, and therefore, a

60-mm-thick model soil layer corresponds to a 3-m-thick soil layer in the prototype scale.

2.4.4 Instrumentation and monitoring

Eight porewater pressure transducers (PPTs) were installed while constructing the model slope. The arrangement of PPTs is illustrated in Fig. 3. These PPTs respond only to the positive porewater pressure. Therefore, changes to the suction were not captured. All the PPTs are connected to the data acquisition system as shown in Fig. 4a. An image analysis technique was employed to examine the deformation process of the slopes. For this purpose, HAS-U2 Mono high-speed camera with VHF8M-MP wide-angle lens was used which was mounted on the centrifuge arm firmly (Fig. 4). The front view of the experimental setup was illuminated using 06 powerful lights (Fig. 4). Since Masado soil has an unidentifiable soil texture, a set of markers is placed covering the focus area of the slope in between the soil slope and the transparent window during the slope construction to capture the mechanical response of the slopes (Fig. 4b). Each side of the markers has a dimension of 10 mm and a thickness of 1 mm. These markers were arranged not to overlap during the initial slope movements. Before the test, the lens was adjusted to focus on the markers to reach the best view. The markers were firmly getting fitted during the spinning up; thus, there was no relative motion observed. The videos taken from the high-speed camera have 30 frames per second with a resolution of 1920 × 1080. Using the commercial software Dipp Motion [14], pixel coordinates for each marker in horizontal (x) and vertical (y) directions were traced to quantify the displacements of slopes. Pixel coordinates were calibrated to obtain displacements in x and y directions using a known length of the model [14]. x and y displacements obtained from the image analysis were interpolated to a 5 mm × 5 mm finer mesh to accomplish a dense displacement field [51, 52].

3 Numerical simulation

The slope behavior discussed in the experimental program included simultaneous responses of hydrological and mechanical behaviors. Therefore, to further interpret the centrifuge experiment results and to study landslide progression and characteristics of unsaturated soil slopes, a three-phase coupled hydromechanical FEM program was utilized. It has been employed by many researchers to study the unsaturated slopes subjected to rainfall infiltration and presented better performance and applicability using FEM programs [7, 30, 31, 55]. The development of three-phase coupled hydromechanical analysis has been greatly facilitated by the proposed porous media theories [4, 5]. This method has been successfully assessed not only in rainfall-induced slope failures [10, 50] and dynamic response of slopes and embankments [26, 42] but also in the slopes subjected to post-earthquake rainfall [52]. The simplified governing equations of the in-house FEM code employed the momentum balance equation of soil–water–air phases, and the mass and momentum balance equations of porewater, and pore-air [42]. The weak forms of the governing equations were generated using the Galerkin method, and it is composed of three primary variables, namely, soil skeleton velocity (v^s), porewater pressure (p^w) and pore air pressure (p^a). These weak forms were linearized and solved by the Newton–Raphson method. The effective skeleton stress tensor (σ') which is expressed as $-\sigma' = -\sigma - p^a I + s^w(p^a - p^w)I$ adopting the generalized Bishop's formula [16, 23]. s^w is the degree of saturation, which was taken as the weighting factor to characterize the unsaturated soil behavior, and I is the second-order unit
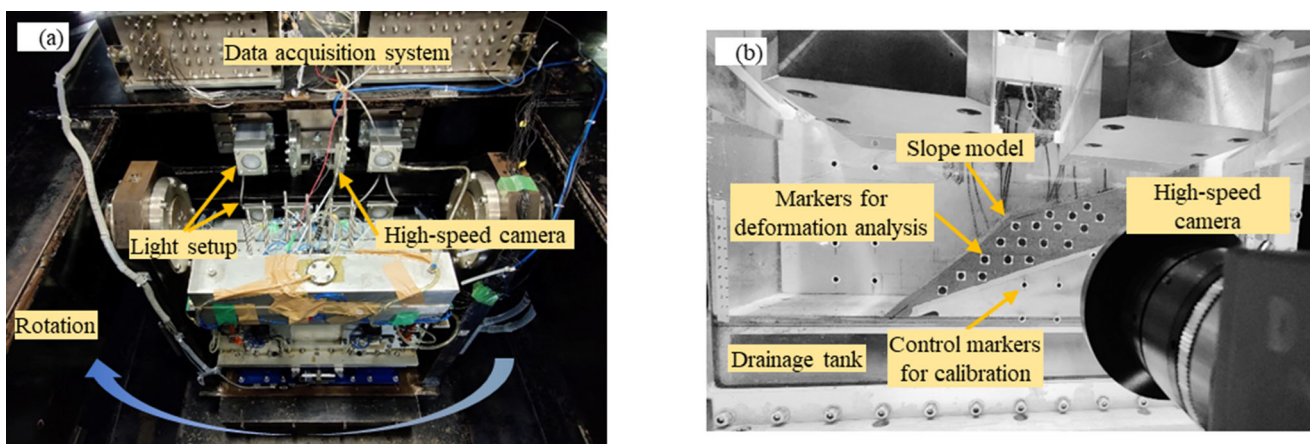
Fig. 4 **a** Experimental setup of the centrifuge model and **b** view of the slope model captured from the high-speed camera and markers' positions for deformation analysis

tensor. The performance of the FEM program was evaluated by comparing the results of experimental data, and thereby analysis was extended to foresee the slopes' behavior under antecedent intermittent rainfall patterns.

3.1 Simulation of water retention behavior

The van Genuchten (VG) model was used to derive the soil water characteristic curve (SWCC) to simulate the water retention behavior [44]. The degree of water saturation (s^w) is expressed as follows:

$$s^w = s_r^w + (s_s^w - s_r^w)s_e^w \quad (1)$$

$$s_e^w = \{1 + (ap^c)^n\}^{-m} \quad (2)$$

where s_r^w and s_s^w are the residual (minimum) and saturated (maximum) degree of saturation, p^c is the suction; s_e^w is the effective water saturation; a, n, and m are the material parameters. A laboratory test was conducted using pressure plate apparatus to determine the soil water characteristic curve (SWCC) of Masado soil. Figure 5 presents the predicted behavior of Eq. 2 as compared to the experimental results in both drying and wetting paths. It shows that the SWCC model employed can capture the hydraulic behavior of soil. However, only the wetting path SWCC is considered in this analysis, and the parameters used for the prediction are reported in Table 3. The permeability coefficients for water (k^{ws}) and air (k^{as}) are assumed to correlate with effective water saturation as Eqs. 3 and 4, respectively, where ξ and η are material parameters and the values used in the analysis are shown in Table 3.

$$k^{ws} = k_s^{ws}\{s_e^w\}^\xi \left[1 - \left\{1 - \left(s_e^w\right)^{\frac{1}{m}}\right\}^m\right]^2 \quad (3)$$

$$k^{as} = k_s^{as}(1 - s_e^w)^\eta \left\{1 - \left(s_e^w\right)^{\frac{1}{m}}\right\}^{2m} \quad (4)$$
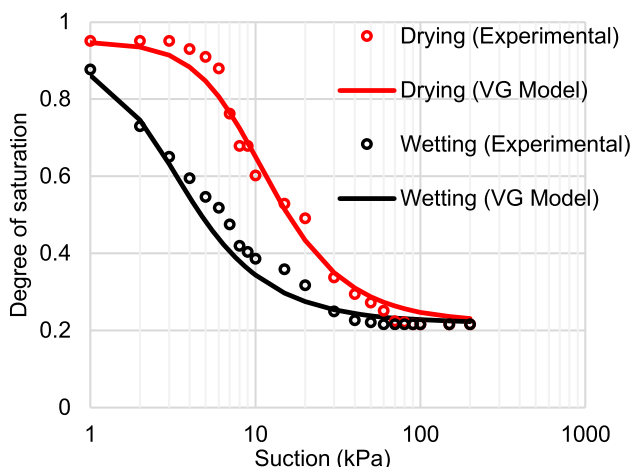

Fig. 5 Measured and predicted SWCC for drying and wetting paths for Masado soil

Table 3 SWCC parameters for Masado soil for wetting path

Parameter	Value
Minimum water saturation S_r	0.25
Maximum water saturation S_w	0.91
Parameter of VG model (a)	0.41
Parameter of VG model (n)	2.2
Parameter of VG model (m)	0.55
Parameter of VG model (ξ)	0.50
Parameter of VG model (η)	0.33

3.2 Simulation of mechanical behavior

To model the mechanical behavior of unsaturated soil, the modified Cam-Clay model is extended to combine the effect of suction on the yield function of unsaturated soil [43]. The yield function postulated to show the effect of suction has the following form.

$$F = F(P, Q, P_c) = \frac{Q^2}{M^2} + [P(P - \overline{P}_c)]$$
$$= \frac{Q^2}{M^2} + \left[P\left(P - \frac{\widetilde{P}_c}{R^*}\right)\right] \quad (5)$$

where P and Q are the mean and deviatoric Kirchhoff effective stress invariants; $\overline{P}_c$ is the Kirchhoff pre-consolidation pressure for unsaturated soil; $\widetilde{P}_c$ is the Kirchhoff pre-consolidation pressure for saturated soil; M is the critical state stress ratio; and R^* is the similarity ratio. The similarity ratio computed the expansion of pre-consolidation pressure with suction. It is a function of suction and degree of water saturation and is expressed as

$$R^* = \exp\left\{-a^c\left[\frac{s^w\theta^c}{p^*}\right]^{b^c}\right\} \quad (6)$$

where θ^c is the Kirchhoff suction; p^* is the reference pressure; a^c and b^c are material parameters controlling the water saturation effect on the yield function; R^* shall be equal to unity when θ^c is less than zero. The evolution law for the hardening parameter can be derived as

$$\overline{P}_c = \frac{\widetilde{P}_c}{R^*} = P_o'\exp\left\{\left(-\frac{1}{(\widehat{\lambda} - \widehat{\kappa})}\varepsilon_v^p\right) + a^c\left[\frac{s^w\theta^c}{p^*}\right]^{b^c}\right\} \quad (7)$$

by assuming $\frac{\Delta\widetilde{P}_c}{\Delta\varepsilon_v^p} = -\frac{1}{(\lambda-\kappa)}\widetilde{P}_c$, which describes the evolution of the yield function developed by plastic volumetric strains (ε_v^p), where $\widehat{\lambda}$ and $\widehat{\kappa}$ are the slopes from the normal consolidation line and unloading and reloading line. A

pressure-dependent hyperelastic model was employed as the elastic stress–strain relationship [6] and additionally subloading surface concept was introduced to describe a smooth transition from the over-consolidation state to the normal consolidation state [53].

The extended modified Cam-Clay model was calibrated for Masado soil based on the experimental results reported using saturated undrained strain-controlled triaxial compression tests (monotonic loading) [52]. The critical state stress ratio ($M = q/p'$) of 1.62 at the onset of large deformations and the corresponding critical state friction angle of 40° was determined. Implicit stress integration was employed to model stress–strain behavior and to calibrate the material parameters used in the numerical simulation study [6]. This method is known as "element simulation". The strain conditions during element simulation were set as $\varepsilon_1 = \varepsilon_3, \varepsilon_1 + \varepsilon_2 + \varepsilon_3 = 0$, and $\varepsilon_{1,2} = 0$ where ε_1 and ε_3 indicate the radial strains and ε_2 indicates the axial strain while $\varepsilon_{1,2}$ notates the shear strain. The initial values of all strain components were set to zero. The stresses were set at 50 kPa in axial and radial directions, while shear stress was set at 0 kPa at the start of the simulation. Experimental data are compared in Fig. 6 with element simulation results, and the parameters used for the calibration are shown in Table 4. Figure 6a shows the stress path ($p' - q$), and Fig. 6b shows the stress–strain behavior. Even though comparisons show slight deviations between the

Table 4 Material parameters for Masado soil

| Parameter	Value
Compression index, tangent of elastoplastic ln v − ln P, $\widehat{\lambda}$	0.05
Swelling index, tangent of elastic ln v − ln P, $\widehat{\kappa}$	0.025
Elastic shear modulus, μ_0	10 kPa
Elastic shear modulus parameter, μ_1	120
Reference elastic volumetric strain ε_{v0}^e	0
Reference mean effective stress, P_0	−1.0 kPa
Ratio of yield stress for mean effective stress at the start of calculation $\widetilde{P_{ct}}/P_i$	1.0
Critical stress ratio, $M = Q/P$	1.62
Isotropic evolution parameter of subloading surface, m_v	0.01
Parameter of unsaturated yield surface, a^c	0.071
Parameter of unsaturated yield surface, b^c	1.6
Parameter of unsaturated yield surface, p_{ref}	1.0

experimental and element simulation data, they captured the primary features of the soil behavior to an acceptable level. The material parameters representing the similarity ratio were calibrated during the numerical simulation to reproduce the experimental results.

3.3 Numerical model and boundary conditions

Figure 7 presents the two-dimensional plane strain finite element model used in this analysis, and this numerical model had the same dimensions as the centrifuge experiment setup shown in Fig. 3. The base was not modeled in the simulation, and the soil–base interface was simulated by applying suitable hydraulic and mechanical boundary conditions. In the finite element analysis iso-parametric, eight-node elements were used to create the computational mesh. A dense mesh toward the left side of the slope was modeled with elements having an average span of 10 mm
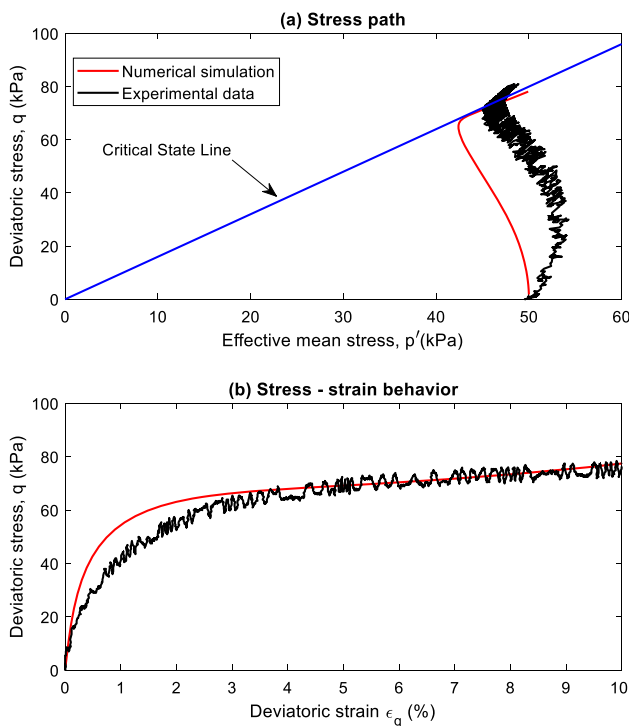
Fig. 6 Comparison between data from undrained triaxial tests on saturated Masado soil and element simulation results using the parameters derived **a** the stress path; **b** the stress–strain behavior
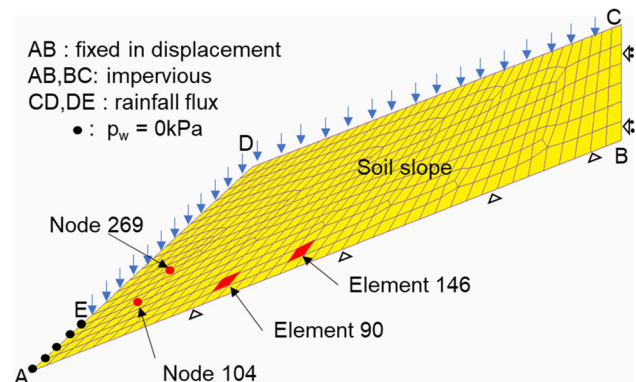
Fig. 7 The two-dimensional finite element model with boundary conditions

on each side. In the eight-node soil skeleton elements, displacement and fluid pressures were assessed at eight-nodes and four-nodes, respectively [42].

As hydrological boundary conditions, rainfall was modeled as flux boundary conditions and was applied on the slope's top surface except for the five bottom nodes along A to E in Fig. 7 which porewater pressures were set to zero to allow the seepage. Additionally, the soil–base interface and the right boundary were considered imper-meable which was analogous to the experimental condi-tions. Air drainage was only allowed on the slope surface, and other boundaries were considered impermeable for the pore air boundary condition. As the displacement boundary condition of the soil skeleton, the nodes along the soil–base interface were fixed in horizontal and vertical directions, while the nodes along the right vertical boundary were set to move freely to avoid the development of tension stress.

3.4 Numerical analysis

The material parameters shown in Tables 3 and 4 were used to describe the hydromechanical behavior of the soil using the VG model and extended MCC model for unsat-urated soil, respectively. The physical properties used for the numerical simulation are shown in Table 5. Firstly, the initial stress analysis was conducted where the soil model was loaded gradually increasing the gravity from 0g to 50g. An unsaturated soil slope was created after the soil model reached 50g, which was comparable to centrifuge testing. Following the initial stress analysis, rainfall was simulated under time histories of precipitation described in Fig. 1. A few elements and nodes were selected and shown in Fig. 7 to discuss the porewater pressure distributions (Element 90 and Element 146) and displacement variations (Node 104 and Node 269).

Table 5 Physical properties of Masado soil

| Parameter	Value
Initial porosity, n_0	0.43
Intrinsic density of soil particle, ρ^{sR}	2.65 g/cm^3
Intrinsic density of water (ρ^{sR}), air (ρ^{sR})	1.0 g/cm^3
	1.2 × 10^{-3} g/cm^3
Saturated permeability coefficient for water, k_s^{ws}	4 × 10^{-5} m/s
Saturated permeability coefficient for air, k_s^{as}	4 × 10^{-6} m/s
Bulk modulus of water, K^w	2 × 10^6 kPa
Gas parameter, $1/\Theta\overline{R}$	1.25 × 10^{-5} s^2/m^2

4 Analysis of experimental data and numerical simulation results

4.1 Effect of antecedent intermittent rainfall conditions on porewater pressure response

Figure 8 shows the time histories of porewater pressure during the four tests. The porewater pressure distribution of PPT 03 and 05 is shown for discussion purposes, and the response of all PPTs' is included in the supplemental material. Generally, all test cases showed a typical devel-opment of the wetting front and increase in porewater pressure upon rainfall infiltration. The significance of each test was discussed to understand more specific changes in the porewater pressure response attributed to antecedent rainfall patterns. Firstly, during test-01, it received 46.2 mm of continuous rainfall and showed an increase in porewater pressure with time before it failed after 110 s, and as previously stated, this test was considered as the reference test for the rest of the cases. In tests 02, 03 and 04, a total of 225 s (6.5 days in the prototype scale) were considered as the antecedent rainfall period before apply-ing the subsequent continuous rainfall until the failure occurs. The total cumulative rainfall applied in the ante-cedent rainfall in all three tests was the same and equal to 37.8 mm, and it showed different time spans to develop positive porewater pressure.

The effect of antecedent rainfall patterns on the pore-water pressure response was more pronounced in test 03 compared to tests 02 and 04, which suggests that the shorter the gap between antecedent rainfall to continuous rainfall, the quicker the response to porewater pressure. Additionally, a closer look at test 03 revealed that positive porewater pressure started building up near PPT 03 during the no-rainfall period (around 215 s) caused by the rainfall infiltration toward the toe area from the antecedent rainfall. Porewater pressure developed constantly with the contin-uous rainfall after 225 s as there was no considerable gap like in test 04. What is interesting in test 04 is that it illustrated the increase in porewater pressure after three antecedent rainfall events and started diminishing of porewater pressure toward zero during the 60 s of the no-rainfall gap. By comparing with the other two cases, test 04 received the total cumulative rainfall just in 165 s, whereas for tests 02 and 03, it took 180 s and 195 s, respectively. This justifies the possibility of developing and diminishing porewater pressure in test 04. More investigation between test 03 and test 04, which correspond to the shortest and the longest gap between the antecedent rainfall to continuous rainfall, suggested the possibility of generating a positive porewater pressure after antecedent rainfall conditions. But depending on the length of the gap (no rainfall) before the
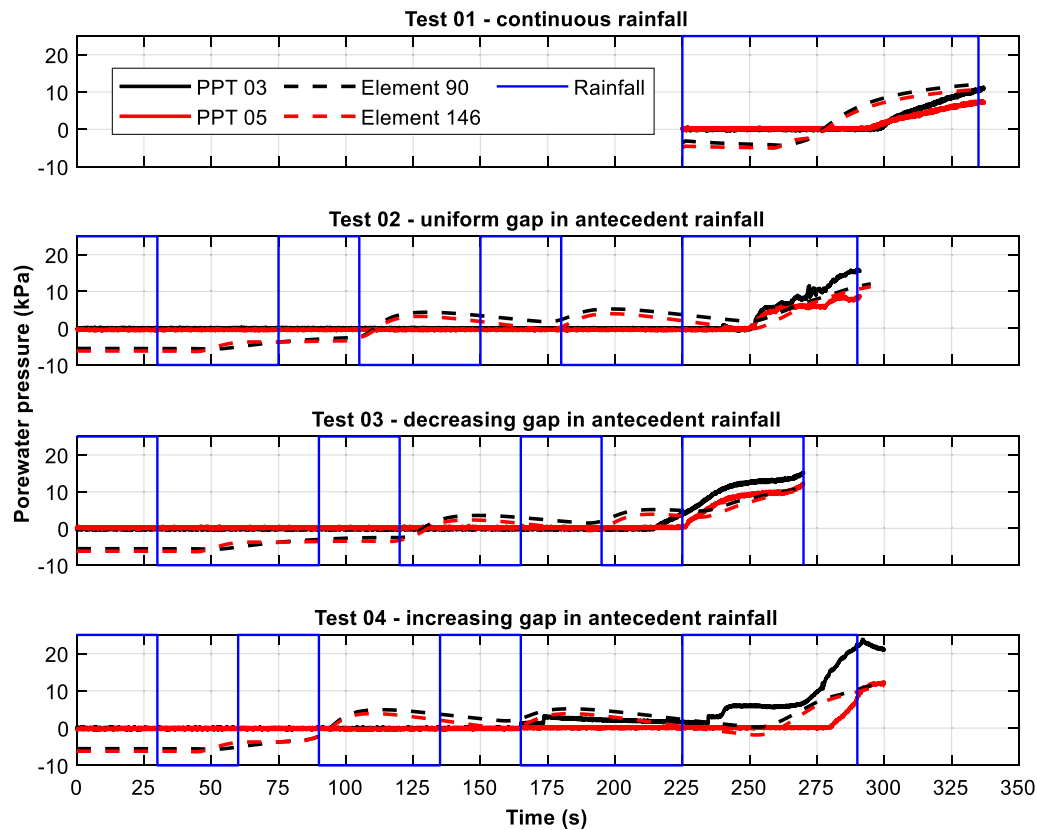
Fig. 8 Porewater pressure response of experimental results and numerical results together with rainfall patterns applied (solid black and red lines show experimental results, and dashed black and red lines show numerical results) (color figure online)

next rainfall porewater pressure will increase or decrease. These are vital observations concerning the hypothesis of this paper: This implies that not only cumulative rainfall, but also antecedent rainfall patterns can cause a remarkable change in porewater pressure responses in slopes.

Figure 8 additionally presents the comparison of porewater pressure distribution of elements 90 and 146, which are corresponding points of PPT 03 and 05 for each test. Numerical simulation results in tests 02, 03, and 04 portrayed that after the second antecedent rainfall, the slopes lost their negative porewater pressure, then the porewater pressure became positive, and it depleted gradually during the gap between the second and third rainfall events. A similar performance resulted between in third rainfall and continuous rainfall in test 02 and test 04. However, in test 03, the gap between the third and continuous rainfall was not enough to observe the depletion of porewater pressure. The evolution of positive porewater pressures during the antecedent rainfall conditions, as produced in numerical simulations, was not exhibited practically in model tests except between the third and continuous rainfall in test 04. This might be because PPTs could not always be responded to such a small transient increase in porewater pressure

which did not last for a longer time. However, test 03 would also have shown a similar response of positive porewater pressure as in a heap if there was more gap before the continuous rainfall. This means it is possible to generate and deplete positive porewater pressure in the events of antecedent rainfall periods depending on the patterns in which numerical simulations are captured successfully. Despite the differences in the antecedent rainfall period, comparisons provide an overall fair representation between the numerical and experimental results during the continuous rainfall period until the failure in all test cases. The plots in Fig. 9 compare the porewater pressure distribution of the entire slope at 225 s of tests 02, 03, and 04 and indicate the initial conditions before the slopes experience continuous rainfall. It clearly shows that substantial porewater pressure seems to be built up at the soil–base interface in test 03 compared to tests 02 and 04. Figure 9d–f, demonstrates that at the time of complete failure, the porewater pressure of different cases showed a similar distribution. These satisfactory results further validate the hydrological parameters used in the numerical simulation.
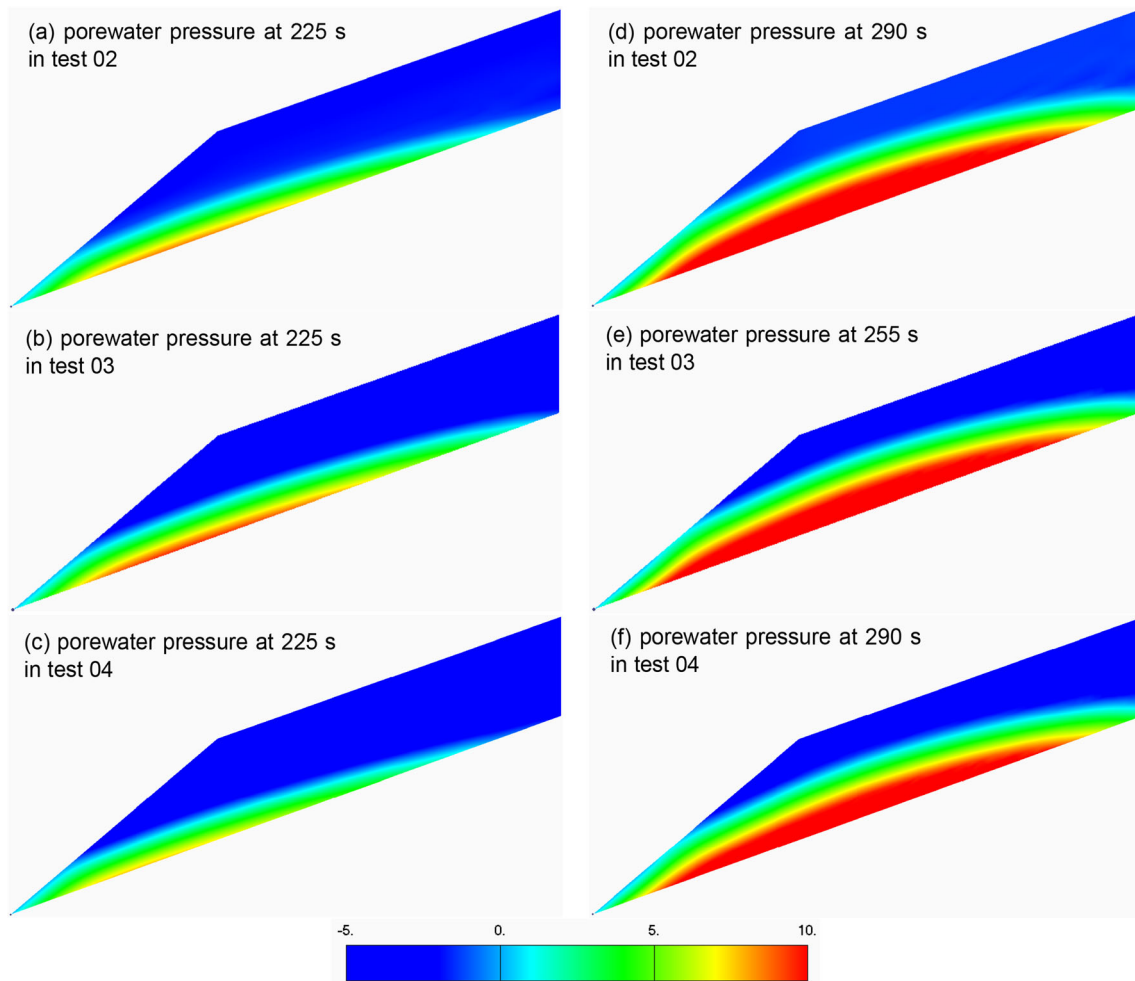
Fig. 9 Porewater pressure variation of soil slope from numerical simulation in tests 02, 03, and 04 at 225 s (**a–c**) and the failure times (**d–f**)

4.2 Deformation characteristics of slopes subjected to antecedent intermittent rainfall conditions

4.2.1 Observations

It was ensured that during the centrifuge experiments, the landslide characteristics could be caught using a high-speed camera, enabling further quantitative analysis of displacements using image analysis. Figure 10a shows the initial failure surface developed in test 03, while Fig. 10b illustrates the vectors of total displacement at the time of failure, and it shows that dense arrow concentration toward the toe of the slope. In general, the initial failure profiles in all four test cases are mostly equivalent to Fig. 10a, even though the initial failure has occurred in different periods. Further, progressive failures of slopes were observed following the initial failure. Figure 10c presents numerical simulation results of the resultant displacement distribution at the time of failure in test 03. It demonstrates that the

displacements are concentrated toward the toe region of the slope and the initial failure surfaces tend to be a thin slice of the slope, which is similar to the experimental case.

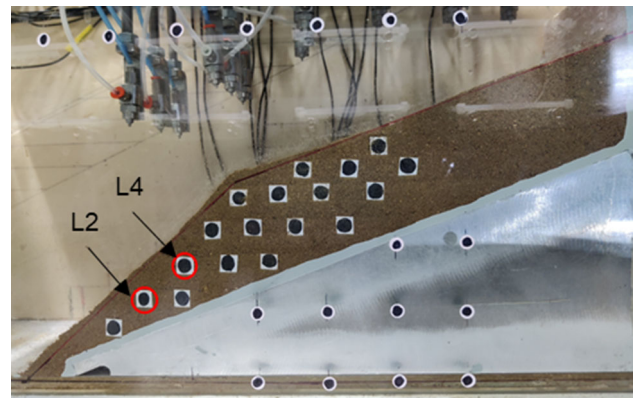### 4.2.2 Displacement and incremental velocity analysis

To illustrate the displacement behavior, two points were selected, namely L2 and L4, as shown in Fig. 11. The displacements were calibrated relative to the toe of the slope, and if the movements are leftwards and downwards, displacements are defined as positive. The progression of landslide with a comparison between horizontal displacements corresponding to L2 and L4 points is shown in Fig. 12. It is worth noting that only test 03 (Fig. 12b, e) shows some displacement compared to tests 02 and 04 at the end of three rainfall events, even though the cumulative rainfall was similar. It was another signal that the antecedent rainfall conditions in test 03 are more vulnerable compared to tests 02 and 04. The displacements of points gradually increased with the continuous rainfall and test 03

(a)

(b)

(c)
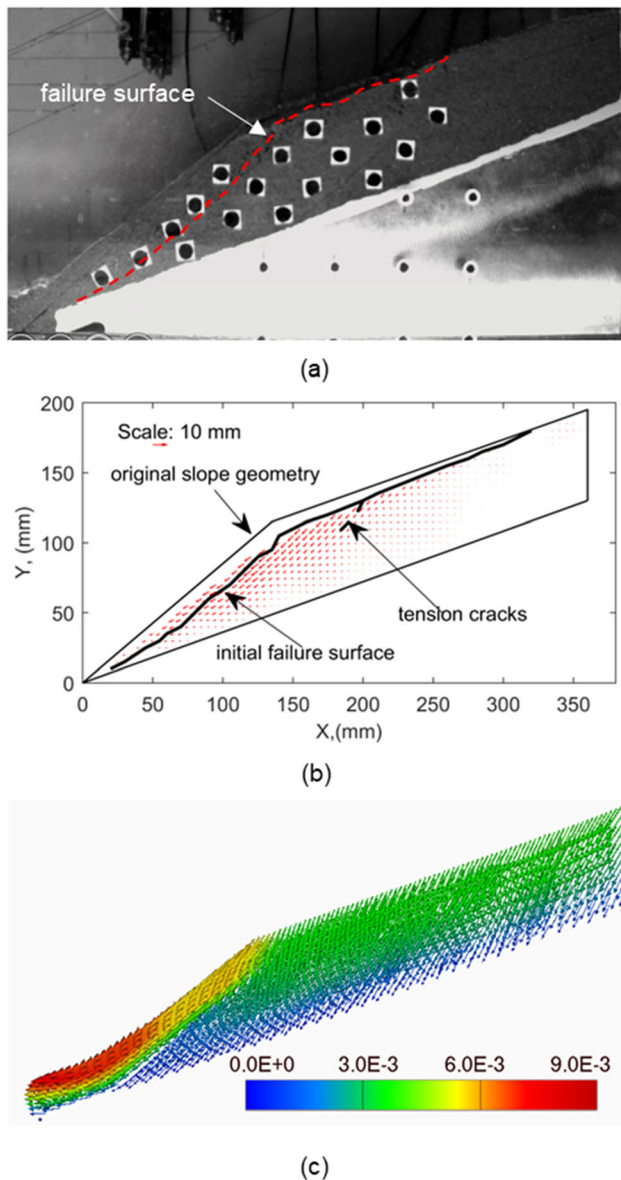
Fig. 10 Initial failure surface in test 04. **a** Image from test 03 showing the failure surface; **b** arrow diagram showing the tendency of failure; **c** numerical simulation results of the resultant displacement

Fig. 11 Markers position of L2 and L4 for displacement analysis

showed a quicker response and eventually failed. This can be attributed to the closer gap between continuous rainfall and immediate rainfall event.

Evolution of displacements of corresponding points in experimental (L2 and L4) and numerical simulations (node 104 and 269) are also compared in Fig. 12. In test 03, the experimental case exhibits a gradual increase in horizontal displacement from 200 s onwards, but numerical simulation result did not reproduce such a gradual change, yet it successfully reproduced the displacement behavior at the period of failure, i.e., around 250 s. Additionally, comparing the overall results revealed that the first signs of significant displacements are exhibited at similar time

intervals following insignificant displacements. However, in the case of experimental results, it showed an exponential increase in displacement at a higher pace probably after the failure was initiated, whereas in the numerical simulation, a similar displacement profile was exhibited in test 03. Nevertheless, the calculated displacement results show numerical simulations successfully reproduced the displacement behavior at the corresponding times in each test case. These results validated the calibrated material parameters used for the similarity ratio (R^*) as well.

The time history of incremental velocity was evaluated to determine the periods of momentous instances of slope behavior. Figure 13 presents the time histories of the incremental horizontal velocity of L2 and compares the incremental velocity variation between experimental and numerical results. The numerical results did not reproduce the smaller peaks, but they properly captured the notable high spikes shown in the experimental results. The timings of failure initiation were quantitatively interpreted by the high spikes in incremental velocity values. Especially in test 03, it was observed that failure initiation took place at 250 s, while the slope failed quickly following the gradual increase in velocity at 255 s. This observation of continuous increase in incremental velocity was not reproduced in numerical results. However, incremental velocity values and the timings of failure initiation generated from numerical simulation results are analogous to experimental results. Accordingly, at the appearance of high spikes, failure initiation took in the order of test 03, test 02, and test 04, which is analogous to decreasing, uniform, and increasing gaps between antecedent rainfall events.

4.2.3 Deviatoric strain analysis

Prefailure deformation [9, 24] analysis is more important to identify the effect of cumulative rainfall and its intermittent behavior on landslide initiation. Strain analysis was
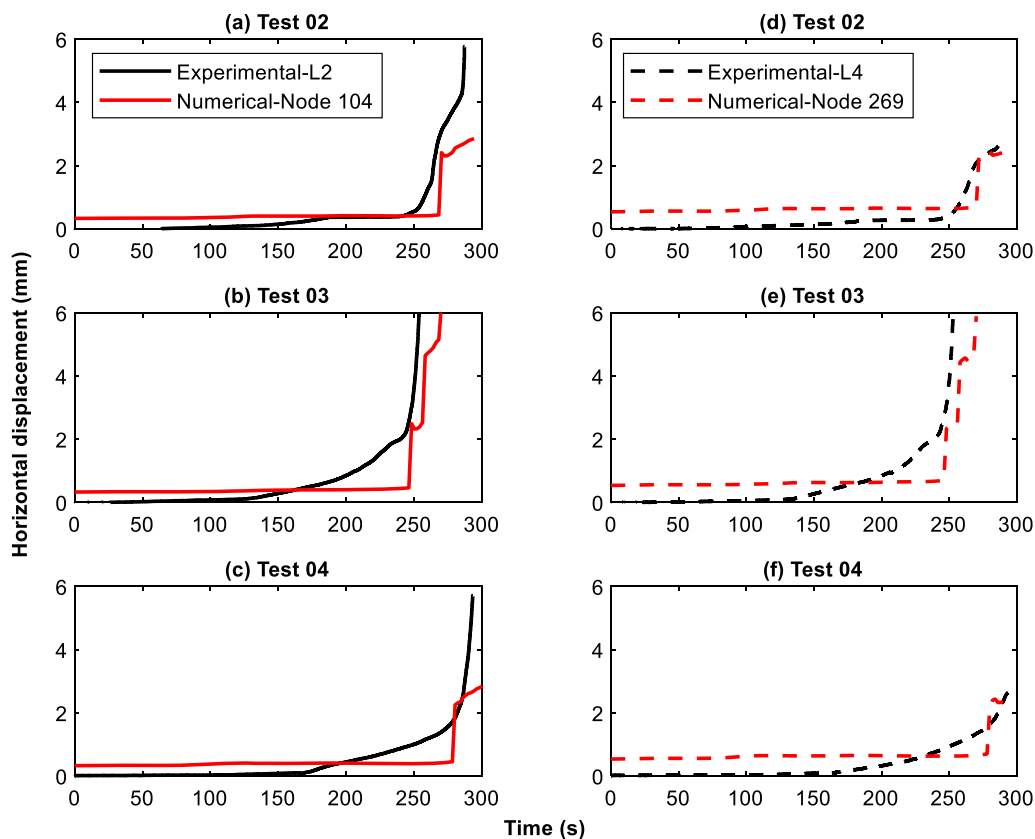
Fig. 12 Evolution of displacement **a–c** L2 of experiment results and Node 104 of numerical results; **d–f** L4 of experiment results and Node 269 of numerical results

conducted to further investigate the pre-failure deformation in critical time steps. The horizontal and vertical displacements determined by the image analysis were utilized to calculate the strain values. In the computation, the slope was assumed to be comprised of square soil elements (Fig. 14) of each side's length of 'a' and the strain components can be computed from the following Eqs. 8,9 and 10 [57]:

$$\varepsilon_{xx} = \frac{1}{2a}(u_4 + u_1 - u_2 - u_3) \tag{8}$$

$$\varepsilon_{yy} = \frac{1}{2a}(v_2 + v_1 - v_4 - u_3) \tag{9}$$

$$\varepsilon_{xy} = \frac{1}{2a}\{(u_1 + u_2 - u_3 - u_4) + (v_1 + v_4 - v_2 - u_3)\} \tag{10}$$

where ε_{xx}, ε_{yy} and ε_{xy} are the horizontal and vertical normal strain and shear strain, respectively. u and v are the nodal displacements in horizontal and vertical directions, as shown in Fig. 14, and the subscripts represent the node number. Since the centrifuge experiments conducted in this series were considered plane strain conditions, the deviatoric strain has the following form [51]

$$\varepsilon_d = \sqrt{\frac{2}{3}}\sqrt{\left(\varepsilon_{xx} - \frac{\varepsilon_v}{3}\right)^2 + \left(\varepsilon_{yy} - \frac{\varepsilon_v}{3}\right)^2 + 2\varepsilon_{xy}^2} \tag{11}$$

where ε_v is the volumetric strain and $\varepsilon_v = \varepsilon_{xx} + \varepsilon_{yy}$

Figure 15 illustrates and compares the deviatoric strain progression of the slope movements at three momentous instances throughout each test with the help of incremental velocity graphs, namely, (i) end of antecedent rainfall period (at 225 s), (ii) failure initiation, and (iii) time of complete failure. Figure 15a1, b1, and c1 indicates that no significant movement has yet begun in any of the test cases at the end of the antecedent rainfall. A closer view shows that a small local strain accumulation has appeared at the toe area of test 03 at 225 s (Fig. 15b1) in the soil–base interface suggesting the earlier initiation of deformation. What is apparent from this is that the antecedent rainfall condition experienced by test 03 is more vulnerable compared to the other two rainfall conditions, which is an important observation of the hypothesis of this study. Figure 15a2, b2, and c2 shows the evolution of the initial failure surfaces, which developed from the toe area and propagated toward the crest of the slope. Figure 15 (b2) very clearly demonstrates that strain localization and causing the failure surface in test 03 contrasted to the other
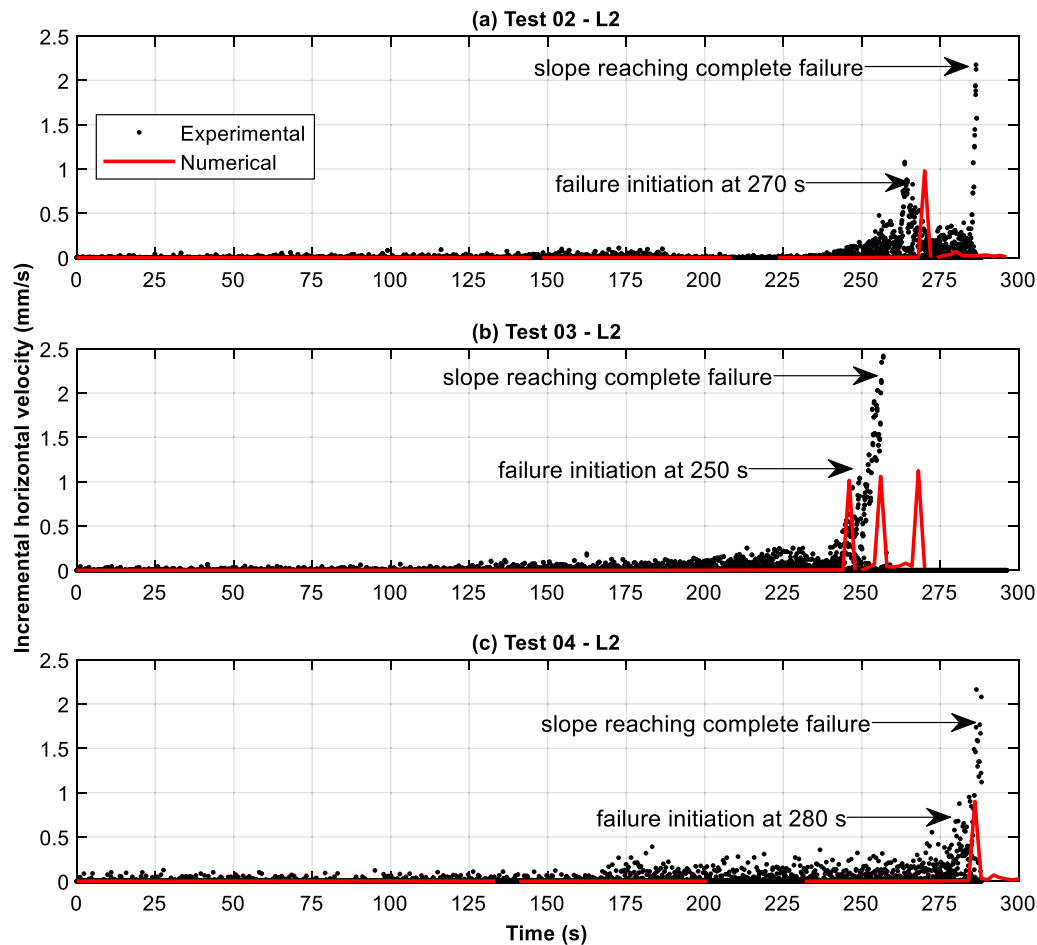
Fig. 13 Variation of the incremental velocity of L2 compared with Node 104 **a** Test 02, **b** Test 03, and **c** Test 04
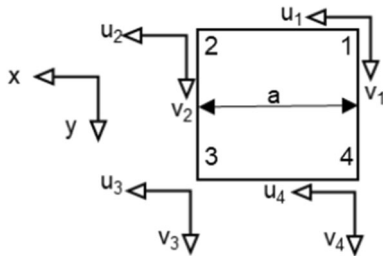

Fig. 14 Soil element selected for strain analysis

two tests. Figure 15a3, b3, and c3 illustrates the numerical simulation results at the times of failure initiation and provide a clear view of localized deformations from the soil–base interface to the surface of the slope. This suggested that a larger time interval between antecedent rainfall and the following continuous rainfall will lead to a more delayed occurrence of landslide initiation. Figure 15a4, b4, and c4 shows the deviatoric strain plots at the time of failure, which distinctly demonstrates the slip surface. Particularly, in Fig. 15b4, it is shown that the second failure surface was set in motion because of the loss

of toe support. Numerical analysis results (Fig. 15a5, b5, and c5) show the expanded failure surfaces with time, and those were comparable to the experimental results. The above evidence and discussion imply that antecedent rainfall patterns could make an impact on landslide initiation timings; hence, similar attention should pay as same to cumulative rainfall.

5 The relative importance of antecedent rainfall conditions for landslide initiation

The analysis was extended further to examine the importance of rainfall intermittent behavior for the landslide initiation process by predicting the failure initiation time based on the evolution of deviatoric strain in numerical simulation. Firstly, the analysis was conducted by varying each gap in turn by keeping the other two gaps as the original case (Fig. 1) of the antecedent rainfall period in test 03, as shown in Fig. 16a, to quantitatively analyze the time for failure initiation. The total cumulative rainfall was the same as the previous study and equal to 90 s of rainfall.
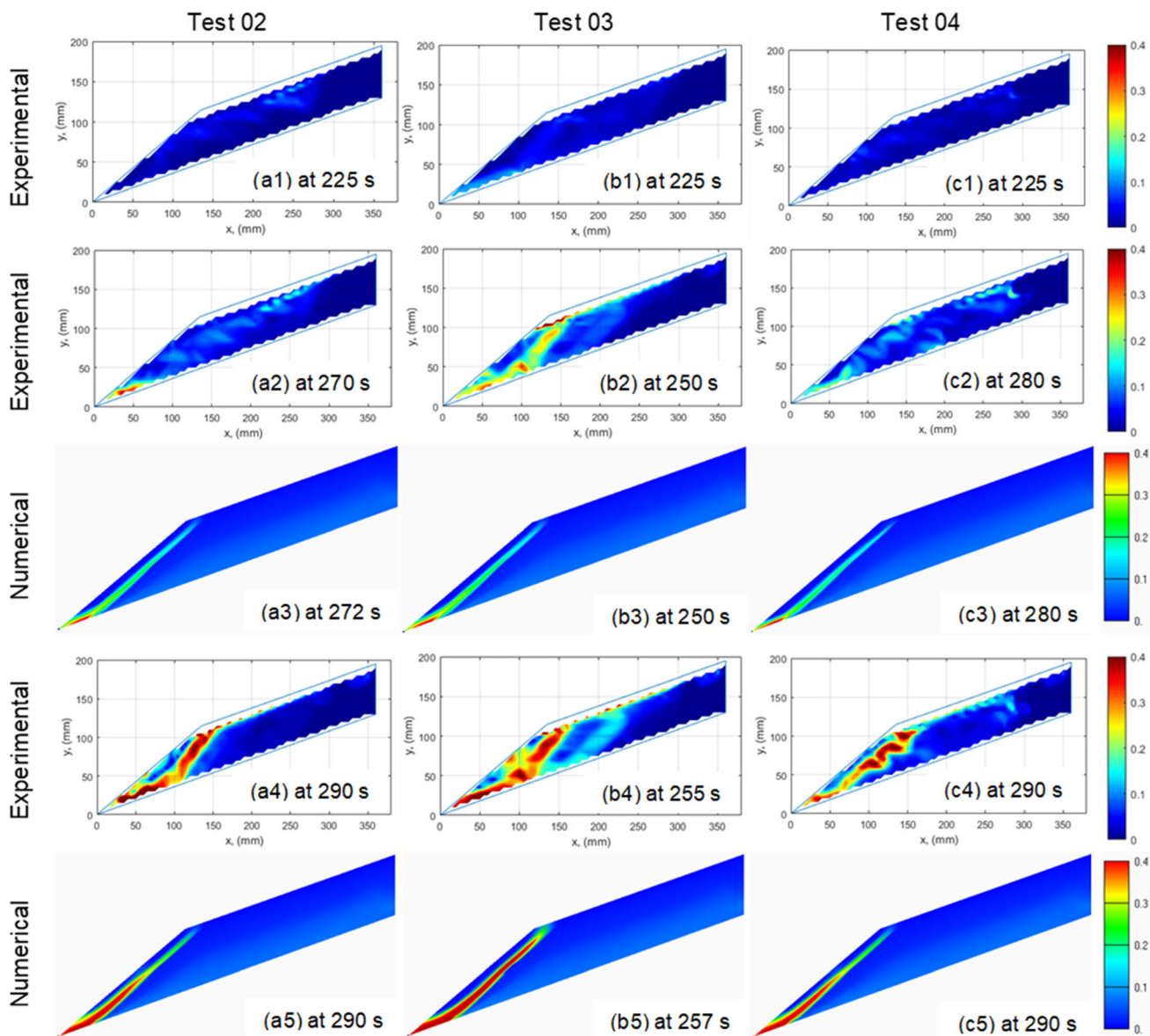
Fig. 15 Distribution and comparison of deviatoric strains at (i) end of antecedent rainfall period (**a1**, **b1**, and **c1** at 225 s), (ii) failure initiation (**a2**, **b2**, and **c2**) from experiments, (**a3**), (**b3**), and (**c3**) from simulations), and (iii) time of complete failure (**a4**, **b4**, and **c4** from experiments, **a5**, **b5**, and **c5** from simulations)

Figure 16b presents the variation of time for failure and the change of gaps. It clearly showed that changes to gap 03 could make the most significant impact on predicting the failure time, whereas gap 01 and gap 02 show a relatively lower impact. Secondly, Fig. 16c presents the time for the evolution of failure with gap 3 for three different saturated permeability values. Although the permeability values were laid in the same order, it illustrates a major change in failure times. The variation of failure time followed the same trend as Fig. 16c while exhibiting that the higher the permeability, the slower the failure initiation.

Further, it is worth noting that there is an inflection point around 75 s (in Fig. 16b, c) based on the imposed boundary conditions. To assess such variation, porewater pressure distribution of element 90 when gap 02 varied from 45 to 180 s is presented in Fig. 16d. The porewater pressure values at the onset of third antecedent rainfall are also shown. Particularly, when the gap kept increasing the slope tends to reinstate its stability by dissipating the positive porewater pressure and neutralizing the effect of first and second rainfall events. Therefore, failure initiation time almost became a constant and contingent on the third antecedent rainfall and continuous rainfall. This illustrated that the effectiveness of the antecedent rainfall event could be sustained only for a certain period. On the other hand, owing to loss of matric suction and the presence of high
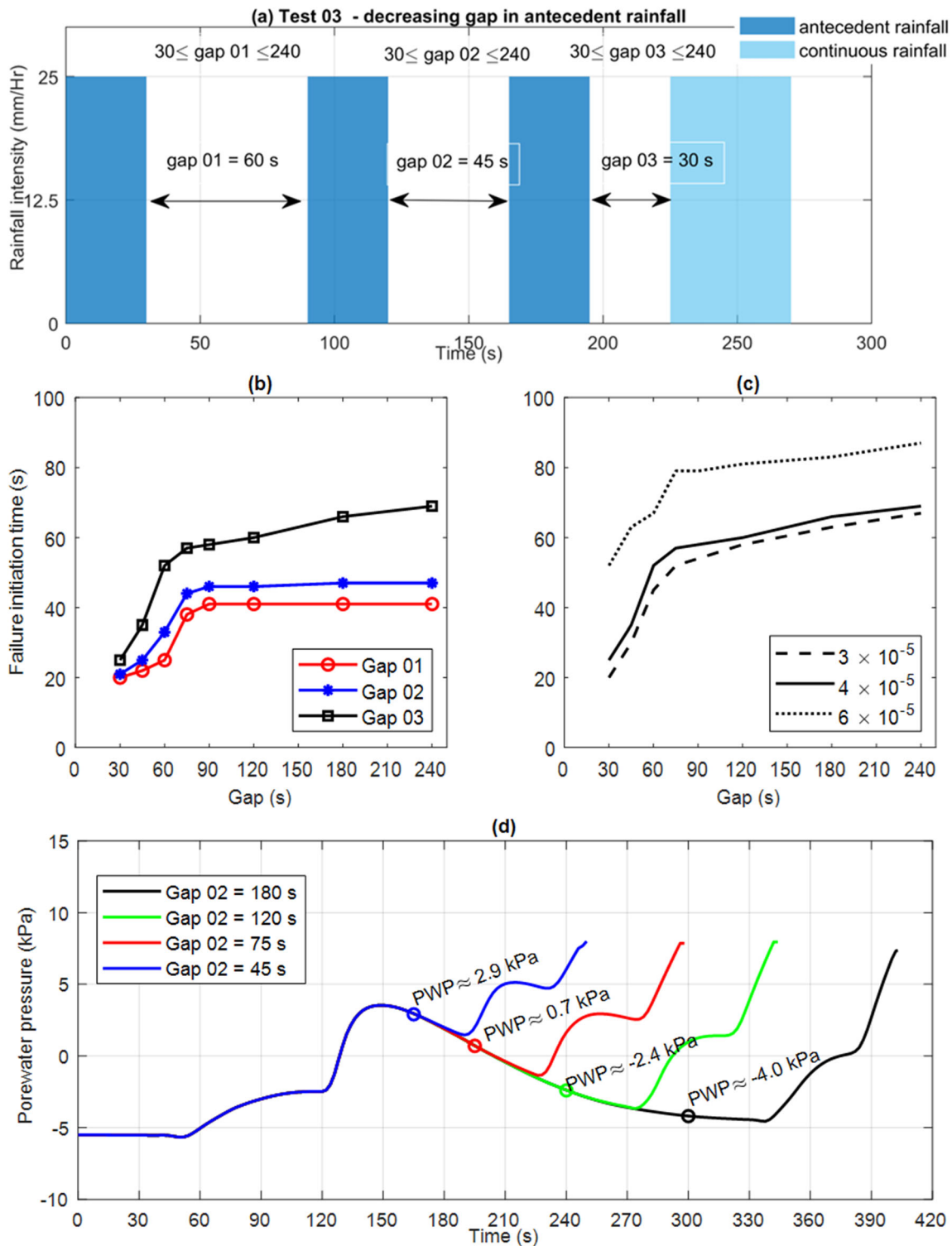
Fig. 16 a The locations of gaps for analysis, **b** The effect of change in gap values for failure initiation time, **c** The effect of change in permeability for failure initiation time, **d** The change of porewater pressure of element 90 with time when gap 02 varies from 45 to 180 s

positive porewater pressure accelerated the failure initiation with the assistance of both first and second rainfall events if the gap values were less than 75 s. Consequently, all three antecedent rainfall events and continuous rainfall

modulated the failure initiation. These findings suggested that there is a possibility to define a critical gap value between two adjoining rainfall events (75 s, in this study) that would influence the initiation time of a landslide. This

value may determine whether the effect of preceding rainfall event should be considered in landslide early warning or not.

6 Summary and conclusions

This study investigates the contribution of intermittent antecedent rainfall conditions on landslide initiation. Out of four centrifuge model tests, three tests were utilized to discuss the behavior of silty sand slopes subjected to similar cumulative rainfall but different antecedent rainfall patterns. The hydraulic and mechanical responses of slopes were thoroughly examined and compared with a three-phase two-dimensional coupled hydromechanical FEM analysis.

A total of 225 s were considered as the antecedent rainfall period while three rainfall patterns were applied, namely uniform, decrease and increase during the antecedent rainfall period. Afterward, continuous rainfall was applied on the slopes until the failure was initiated. It has been demonstrated that the decreasing gap rainfall pattern produced the quickest landslide initiation, whereas the slope that experienced the increasing gap rainfall pattern failed at last. Despite that, all the slopes have been exposed to the same amount of cumulative rainfall; these observations suggested antecedent rainfall patterns could have a considerable influence on predicting landslide initiation. Therefore, attention should be focused not only on cumulative rainfall but also on rainfall patterns in landslide early warning mechanisms.

Porewater pressure responses generated from physical model tests and numerical analysis illustrated that the results were analogous. The development of positive porewater pressure with the increase in wetting front and failure emerged, while the increase in porewater pressure was a common observation. However, numerical analysis was used to deeply examine the effect of rainfall patterns on the advancement of porewater pressure in critical times. It portrayed that decreasing gap (test 03) rainfall pattern resulted in a significantly higher porewater pressure in the soil–base interface compared to tests 02 and 04.

Mechanical responses of the slopes were evaluated based on the evolution of displacement, incremental velocity, and deviatoric strain. Centrifuge test results and numerical simulation results showed a very satisfactory agreement by capturing the displacements and strains in the corresponding times. Analysis of mechanical response greatly helped to understand the failure initiation where it exhibited decreasing gap rainfall caused early signs of instability. Deviatoric strain analysis showed that the failure initiated from the toe of the slope and propagated toward the slope crest.

Finally, numerical simulation was extended to recognize the relative importance of each gap. It demonstrated that gap 3 had a prominent impact on predicting the failure time compared to gap 1 and gap 2. Further, it was found that the critical gap value potentially governs the effect of preceding rainfall event to landslide initiation. These results suggested that not only cumulative rainfall, but also antecedent rainfall patterns could be vital for accurately forecasting landslide early warnings. Therefore, predicted rainfall over a critical period could be scrutinized in advance of issuing landslide early warnings to vulnerable communities. In future studies, landslide initiation and its characteristics will be examined particularly under the integrated effect of pre-existing groundwater table and rainfall infiltration to support the predictive models.

Data availability The datasets generated during and/or analyzed during the current study are available from the corresponding author upon reasonable request.

Declarations

Conflict of interest The authors have no competing interests to declare that are relevant to the content of this article.

References

1. Askarinejad A, Akca D, Springman SM (2018) Precursors of instability in a natural slope due to rainfall: a full-scale experiment. Landslides 15:1745–1759. https://doi.org/10.1007/s10346-018-0994-0
2. Askarinejad A, Beck A, Springman SM (2015) Scaling law of static liquefaction mechanism in geocentrifuge and corresponding

hydromechanical characterization of an unsaturated silty sand having a viscous pore fluid. Can Geotech J 52:708–720. https://doi.org/10.1139/cgj-2014-0237

3. Bhattacherjee D, Viswanadham BVS (2018) Design and performance of an in-flight rainfall simulator in a geotechnical centrifuge. Geotech Test J 41:72–91. https://doi.org/10.1520/GTJ20160254

4. Biot MA (1941) General theory of three-dimensional consolidation. J Appl Phys 12:155–164. https://doi.org/10.1063/1.1712886

5. Biot MA (1962) Mechanics of deformation and acoustic propagation in porous media. J Appl Phys 33:1482–1498. https://doi.org/10.1063/1.1728759

6. Borja RI, Tamagnini C (1998) Cam-clay plasticity part III: extension of the infinitesimal model to include finite strains. Comput Methods Appl Mech Eng 155:73–95. https://doi.org/10.1016/S0045-7825(97)00141-2

7. Borja RI, White JA (2010) Continuum deformation and stability analyses of a steep hillside slope under rainfall infiltration. Acta Geotech 5:1–14. https://doi.org/10.1007/s11440-009-0108-1

8. Cai F, Ugai K (2004) Numerical analysis of rainfall effects on slope stability. Int J Geomech 4:69–78. https://doi.org/10.1061/(ASCE)1532-3641(2004)4:2(69)

9. Cascini L, Cuomo S, Pastor M, Sorbino G (2010) Modeling of rainfall-induced shallow landslides of the flow-type. J Geotech Geoenviron Eng 136:85–98. https://doi.org/10.1061/(ASCE)GT.1943-5606.0000182

10. Chen X, Zhang L, Zhang L, Zhou Y, Ye G, Guo N (2021) Modelling rainfall-induced landslides from initiation of instability to post-failure. Comput Geotech 129. https://doi.org/10.1016/j.compgeo.2020.103877

11. Damiano E (2019) Effects of layering on triggering mechanisms of rainfall-induced landslides in unsaturated pyroclastic granular soils. Can Geotech J 56:1278–1290. https://doi.org/10.1139/cgj-2018-0040

12. Dang K, Sassa K, Konagai K, Karunawardena A, Bandara RMS, Hirota K, Tan Q, Ha ND (2019) Recent rainfall-induced rapid and long-traveling landslide on 17 May 2016 in Aranayaka, Kagelle District, Sri Lanka. Landslides 16:155–164. https://doi.org/10.1007/s10346-018-1089-7

13. Dell'Avanzi E, Zornberg JG, Cabral AR (2004) Suction profiles and scale factors for unsaturated flow under increased gravitational field. Soils Found 44:79–89. https://doi.org/10.3208/sandf.44.3_79

14. DITECT Corporation (2017) DIPP-Motion V

15. Fan X, Tang J, Tian S, Jiang Y (2020) Rainfall-induced rapid and long-runout catastrophic landslide on July 23, 2019 in Shuicheng, Guizhou, China. Landslides 17:2161–2171. https://doi.org/10.1007/s10346-020-01454-y

16. Gallipoli D, Gens AA, Sharma R, Vaunat J (2003) An elasto-plastic model for unsaturated soil incorporating the effects of suction and degree of saturation on mechanical behaviour. Géotechnique 53(1):123–135. https://doi.org/10.1680/geot.2003.53.1.123

17. Garnier J, Gaudin C, Springman SM, Culligan PJ, Goodings D, Konig D, Kutter B, Phillips R, Randolph MF, Thorel L (2007) Catalogue of scaling laws and similitude questions in geotechnical centrifuge modelling. Int J Phys Model Geotech 7:01–23. https://doi.org/10.1680/ijpmg.2007.070301

18. Giannecchini R, Galanti Y, D'Amato Avanzi G (2012) Critical rainfall thresholds for triggering shallow landslides in the Serchio River Valley (Tuscany, Italy). Nat Hazards Earth Syst Sci 12:829–842. https://doi.org/10.5194/nhess-12-829-2012

19. Guzzetti F, Peruccacci S, Rossi M, Stark CP (2008) The rainfall intensity-duration control of shallow landslides and debris flows: an update. Landslides 5:3–17. https://doi.org/10.1007/s10346-007-0112-1

20. Ha ND, Sayama T, Sassa K, Takara K, Uzuoka R, Dang K, Van Pham T (2020) A coupled hydrological-geotechnical framework for forecasting shallow landslide hazard: a case study in Halong City, Vietnam. Landslides 17:1619–1634. https://doi.org/10.1007/s10346-020-01385-8

21. Harilal GT, Madhu D, Ramesh MV, Pullarkatt D (2019) Towards establishing rainfall thresholds for a real-time landslide early warning system in Sikkim, India. Landslides 16:2395–2408. https://doi.org/10.1007/s10346-019-01244-1

22. He X, Hong Y, Vergara H, Zhang K, Kirstetter PE, Gourley JJ, Zhang Y, Qiao G, Liu C (2016) Development of a coupled hydrological-geotechnical framework for rainfall-induced landslides prediction. J Hydrol (Amst) 543:395–405. https://doi.org/10.1016/j.jhydrol.2016.10.016

23. Jommi C (2000) Remarks on the constitutive modelling of unsaturated soils. In: Experimental evidence and theoretical approaches in unsaturated soils. CRC Press, pp 147–162

24. Leroueil S (2001) Natural slopes and cuts: movement and failure mechanisms. Géotechnique 51:197–243. https://doi.org/10.1680/geot.2001.51.3.197

25. Ling H, Ling HI, Asce M (2012) Centrifuge model simulations of rainfall-induced slope instability. J Geotech Geoenviron Eng 38. https://doi.org/10.1061/(ASCE)GT.1943

26. Matsumaru T, Uzuoka R (2016) Three-phase seepage-deformation coupled analysis about unsaturated embankment damaged by earthquake. Int J Geomech 16. https://doi.org/10.1061/(asce)gm.1943-5622.0000699

27. Ng CWW, Kamchoom V, Leung AK (2016) Centrifuge modelling of the effects of root geometry on transpiration-induced suction and stability of vegetated slopes. Landslides 13:925–938. https://doi.org/10.1007/s10346-015-0645-7

28. Ng CWW, Shi Q (1998) A numerical investigation of the stability of unsaturated soil slopes subjected to transient seepage. Comput Geotech 01:01–28. https://doi.org/10.1016/S0266-352X(97)00036-0

29. Ng CWW, Zhan LT, Bao CG, Fredlund DG, Gong BW (2003) Performance of an unsaturated expansive soil slope subjected to artificial rainfall infiltration. Géotechnique 53(2):143–157. https://doi.org/10.1680/geot.2003.53.2.143

30. Oh S, Lu N (2015) Slope stability analysis under unsaturated conditions: case studies of rainfall-induced failure of cut slopes. Eng Geol 184:96–103. https://doi.org/10.1016/j.enggeo.2014.11.007

31. Qi S, Vanapalli SK (2015) Hydro-mechanical coupling effect on surficial layer stability of unsaturated expansive soil slopes. Comput Geotech 70:68–82. https://doi.org/10.1016/j.compgeo.2015.07.006

32. Rahardjo H, Lee TT, Leong EC, Rezaur RB (2005) Response of a residual soil slope to rainfall. Can Geotech J 42:340–351. https://doi.org/10.1139/t04-101

33. Rahardjo H, Ong TH, Rezaur RB, Leong EC (2007) Factors controlling instability of homogeneous soil slopes under rainfall. J Geotech Geoenviron Eng 133:1532–1543. https://doi.org/10.1061/(ASCE)1090-0241(2007)133:12(1532)

34. Rahimi A, Rahardjo H, Leong E-C, Asce M (2011) Effect of antecedent rainfall patterns on rainfall-induced slope failure. https://doi.org/10.1061/(ASCE)GT.1943-5606.0000451

35. Sasahara K, Sakai N (2014) Development of shear deformation due to the increase of pore pressure in a sandy model slope during rainfall. Eng Geol 170:43–51. https://doi.org/10.1016/j.enggeo.2013.12.005

36. Take WA, Beddoe RA (2014) Base liquefaction: a mechanism for shear-induced failure of loose granular slopes. Can Geotech J 51:496–507. https://doi.org/10.1139/cgj-2012-0457

37. Take WA, Beddoe RA, Davoodi-Bilesavar R, Phillips R (2015) Effect of antecedent groundwater conditions on the triggering of

static liquefaction landslides. Landslides 12:469–479. https://doi.org/10.1007/s10346-014-0496-7

38. Take WA, Bolton MD, Wong PCP, Yeung FJ (2004) Evaluation of landslide triggering mechanisms in model fill slopes. Landslides 1:173–184. https://doi.org/10.1007/s10346-004-0025-1

39. Tamate S, Suemasa N, Katada T (2012) Simulation of precipitation on centrifuge models of slopes. Int J Phys Model Geotech 12:89–101. https://doi.org/10.1680/ijpmg.11.00009

40. Taylor RN (2018) Geotechnical centrifuge technology. CRC Press

41. Tristancho J, Caicedo B, Thorel L (2015) Mathematical and physical modelling of rainfall in centrifuge. Int J Phys Model Geotech 15:150–164. https://doi.org/10.1680/ijpmg.14.00023

42. Uzuoka R, Borja RI (2012) Dynamics of unsaturated poroelastic solids at finite strain. Int J Numer Anal Methods Geomech 36:1535–1573. https://doi.org/10.1002/nag.1061

43. Uzuoka R, Kazama M, Sento N (2011) Soil–water–air coupled analysis on seepage and overtopping behavior of river levee. In: 14th Asian Regional conference on soil mechanics and geotechnical engineering, ARC 2011

44. van Genuchten MTh (1980) A closed-form equation for predicting the hydraulic conductivity of unsaturated soils. Soil Science Society of America Journal 44:892–898. https://doi.org/10.2136/sssaj1980.03615995004400050002x

45. Wang G, Sassa K (2001) Factors affecting rainfall-induced flowslides in laboratory flume tests. Géotechnique 51:587–599. https://doi.org/10.1680/geot.51.7.587.51386

46. Wang H, Zhang L, Yin K, Luo H, Li J (2021) Landslide identification using machine learning. Geosci Front 12:351–364. https://doi.org/10.1016/j.gsf.2020.02.012

47. Wang S, Idinger G (2021) A device for rainfall simulation in geotechnical centrifuges. Acta Geotech 16:2887–2898. https://doi.org/10.1007/s11440-021-01186-w

48. Wang S, Idinger G, Wu W (2021) Centrifuge modelling of rainfall-induced slope failure in variably saturated soil. Acta Geotech 16:2899–2916. https://doi.org/10.1007/s11440-021-01169-x

49. Xing A, Wang G, Li B, Jiang Y, Feng Z, Kamai T (2014) Long-runout mechanism and landsliding behaviour of large catastrophic landslide triggered by heavy rainfall in Guanling, Guizhou, China. Can Geotech J 52:971–981. https://doi.org/10.1139/cgj-2014-0122

50. Xiong Y, Bao X, Ye B, Zhang F (2014) Soil–water–air fully coupling finite element analysis of slope failure in unsaturated ground. In: Soils and foundations. Japanese Geotechnical Society, pp 377–395. https://doi.org/10.1016/j.sandf.2014.04.007

51. Xu J, Ueda K, Uzuoka R (2022) Evaluation of failure of slopes with shaking-induced cracks in response to rainfall. Landslides 19:119–136. https://doi.org/10.1007/s10346-021-01734-1

52. Xu J, Ueda K, Uzuoka R (2022) Numerical modeling of seepage and deformation of unsaturated slope subjected to post-earthquake rainfall. Comput Geotech 148. https://doi.org/10.1016/j.compgeo.2022.104791

53. Yamakawa Y, Hashiguchi K, Ikeda K (2010) Implicit stress-update algorithm for isotropic Cam-clay model based on the subloading surface concept at finite strains. Int J Plast 26:634–658. https://doi.org/10.1016/j.ijplas.2009.09.007

54. Yang H, Wei F, Ma Z, Guo H, Su P, Zhang S (2020) Rainfall threshold for landslide activity in Dazhou, southwest China. Landslides 17:61–77. https://doi.org/10.1007/s10346-019-01270-z

55. Yang KH, Uzuoka R, Thuo JN, Lin GL, Nakai Y (2017) Coupled hydro-mechanical analysis of two unstable unsaturated slopes subject to rainfall infiltration. Eng Geol 216:13–30. https://doi.org/10.1016/j.enggeo.2016.11.006

56. Yubonchit S, Chinkulkijniwat A, Horpibulsuk S, Jothityangkoon C, Arulrajah A, Suddeepong A (2017) Influence factors involving rainfall-induced shallow slope failure: numerical study. Int J Geomech 17:1–13. https://doi.org/10.1061/(asce)gm.1943-5622.0000865

57. Zhang GA, Qian J, Wang R, Zhang J-M (2011) Centrifuge model test study of rainfall-induced deformation of cohesive soil slopes. Soils Found Jpn Geotech Soc 51:297–305. https://doi.org/10.3208/sandf.51.297

58. Zhuang J, Iqbal J, Peng J, Liu T (2014) Probability prediction model for landslide occurrences in Xi'an, Shaanxi Province, China. J Mt Sci 11:345–359. https://doi.org/10.1007/s11629-013-2809-z